


















Tracing high- z Galaxies in X-rays with JWST and *Chandra*

AIDAN KAMINSKY ¹, NICO CAPPELLUTI ¹, GÜNTHER HASINGER ^{2,3,4}, ALESSANDRO PECA ^{5,6},
CAITLIN M. CASEY ^{7,8,9}, NICOLE E. DRAKOS ¹⁰, ANDREAS FAISST ¹¹, GHASSEM GOZALIASL ^{12,13},
OLIVIER ILBERT ¹⁴, JEYHAN S. KARTALTEPE ¹⁵, ALEXANDER KASHLINSKY ^{16,17,18}, ANTON M. KOEKEMOER ¹⁹,
HENRY JOY MCCRACKEN ²⁰, JASON RHODES ²¹, BRANT E. ROBERTSON ²², MARKO SHUNTOV ^{9,23} AND
JOSEPH STERLING ¹

¹*Department of Physics, University of Miami, Coral Gables, FL 33124, USA*

²*TU Dresden, Institute of Nuclear and Particle Physics, 01062 Dresden, Germany*

³*DESY, Notkestraße 85, 22607 Hamburg, Germany*

⁴*Deutsches Zentrum für Astrophysik, Postplatz 1, 02826 Görlitz, Germany*

⁵*Eureka Scientific, 2452 Delmer Street, Suite 100, Oakland, CA 94602-3017, USA*

⁶*Department of Physics, Yale University, P.O. Box 208120, New Haven, CT 06520, USA*

⁷*The University of Texas at Austin, 2515 Speedway Blvd Stop C1400, Austin, TX 78712, USA*

⁸*Department of Physics University of California Santa Barbara, CA, 93106, CA*

⁹*Cosmic Dawn Center (DAWN), Denmark*

¹⁰*Department of Physics and Astronomy, University of Hawaii, Hilo, 200 W. Kawili St., Hilo, HI 96720, USA*

¹¹*Caltech/IPAC, MS 314-6, 1200 E. California Blvd. Pasadena, CA 91125, USA*

¹²*Department of Computer Science, Aalto University, PO Box 15400, Espoo, FI-00 076, Finland*

¹³*Department of Physics, Faculty of Science, University of Helsinki, 00014-Helsinki, Finland*

¹⁴*Aix Marseille Univ, CNRS, CNES, LAM, Marseille, France*

¹⁵*Laboratory for Multiwavelength Astrophysics, School of Physics and Astronomy, Rochester Institute of Technology, 84 Lomb Memorial Drive, Rochester, NY 14623, USA*

¹⁶*Code 665, Observational Cosmology Lab, NASA Goddard Space Flight Center, Greenbelt, MD 20771, USA*

¹⁷*Dept of Astronomy, University of Maryland, College Park, MD 20742, USA*

¹⁸*Center for Research and Exploration in Space Science and Technology, NASA/GSFC, Greenbelt, MD 20771, USA*

¹⁹*Space Telescope Science Institute, 3700 San Martin Drive, Baltimore, MD 21218, USA*

²⁰*Institut d'Astrophysique de Paris, UMR 7095, CNRS, and Sorbonne Université, 98 bis boulevard Arago, F-75014 Paris, France*

²¹*Jet Propulsion Laboratory, California Institute of Technology, 4800 Oak Grove Drive, Pasadena, CA 91001, USA*

²²*Department of Astronomy and Astrophysics, University of California, Santa Cruz, 1156 High Street, Santa Cruz, CA 95064, USA*

²³*Niels Bohr Institute, University of Copenhagen, Jagtvej 128, 2200 Copenhagen, Denmark*

ABSTRACT

We leverage *JWST* data from the COSMOS-Web Survey in order to provide updated measurements on the auto-power spectrum of the now resolved Cosmic Infrared Background (CIB) and its coherence with the unresolved soft Cosmic X-ray Background (CXB) observed by *Chandra* at $z > 6$. Maps of the CIB in the F277W and F444W NIRCcam filters are constructed with sources fainter than $m_{AB} = 25$ and cross-correlated with the CXB in the [0.5-2] keV band. We find that on scales between 1 and 1000'' the CIB-CXB cross-power in both NIRCcam filters is statistically significant with signal-to-noise ratios (S/N) of 4.80 and 6.20 respectively from redshifts $0 \leq z \leq 13$. In our high- z ($6 \leq z \leq 13$) interval we find coherence in both filters with a S/N of 7.32 and 5.39 respectively. These results suggest that there are X-ray emitting galaxies resolved by *JWST*, including star-forming galaxies (SFGs) and active galactic nuclei (AGNs). We fit the large-scale biasing of the IR sources producing the CIB as a function of z with results consistent with prior measurements and place constraints on the CXB flux and biasing at low- and high- z . The CXB flux measurements presented in this study suggest that approximately 94% of the [0.5-2] keV CXB is resolved, and this value is consistent within 2σ with the complete resolution of the [0.5-2] keV CXB.

Keywords: Cosmic background radiation (317), Large-scale structure of the universe (902), Active galactic nuclei (16), Star formation (1569)

1. INTRODUCTION

The Cosmic Near-Infrared Background (CIB) is the integrated radiation from star formation and other astrophysical processes, such as supermassive black hole (SMBH) accretion, spanning all redshifts. While most of the CIB has been resolved, a component remains from unresolved sources which cluster at large angular scales (Kashlinsky et al. 2005; Kashlinsky et al. 2018). This puzzling excess in the unresolved *Spitzer* and *AKARI* CIB fluctuations with respect to extrapolations from known galaxy populations have been reported by several groups (Kashlinsky et al. 2005, 2012; Cooray et al. 2012; Matsumoto et al. 2011). The nature of this excess has been investigated (Helgason et al. 2012, 2014) and two main solutions have been proposed: (1) a high- z signal originating from Population III stars in primordial galaxies (Kashlinsky et al. 2005; Kashlinsky et al. 2025) and (2) a $z \sim 1-4$ signal from Intra-Halo Light (IHL), the result of stripped material (gas and stars) from galaxy mergers (Cooray et al. 2012).

Uncovering the origins behind this excess in the CIB requires knowing the properties of faint galaxies detected in the IR, such as their redshifts, star formation histories, and black hole activity. In the age of the *James Webb Space Telescope (JWST)*, it is possible to resolve the CIB above $1 \mu\text{m}$ into discrete sources down to $m_{AB} \sim 30$, allowing for a better understanding of the populations imprinted on the faint CIB fluctuations.

On the other hand, the Cosmic X-ray Background (CXB) (Giacconi et al. 1962) is the result of the cumulative X-ray emission dominated by accretion onto SMBHs with a small fraction attributed to normal galaxies. X-ray surveys with *ROSAT*, *Chandra* and *XMM-Newton* resolved $>90\%$ of it into discrete point-sources (Hickox & Markevitch 2007; Moretti et al. 2012; Cappelluti et al. 2017a). The nature of the unresolved $<10\%$ CXB and its exact recipe is still debated (Cappelluti et al. 2012a; Helgason et al. 2014) in particular when it comes to determining the contribution of high- z ($z>6$) SMBH accretion. Understanding this is critical, a measurement of such emission at high- z can inform us on the nature of SMBH seeds and the potential contributions of accretion on the reionization of the Universe.

Interestingly, it has been discovered that the unresolved CIB anisotropies show a high level of coherence at large angular scales ($\sim 1000''$) with those of the unresolved *Chandra* [0.5-2] keV CXB (Cappelluti et al. 2013, 2017b; Mitchell-Wynne et al. 2016; Li et al. 2018).

The origin of the CIB-CXB coherence has been a matter of debate and several explanations have been proposed. These include X-ray binary emission in star-forming galaxies (SFGs) and obscured active galactic nuclei (AGNs), both populations being unresolved by *Spitzer* and *Chandra*. Specifically in the high- z regime, primordial black holes (PBHs) (Kashlinsky 2016; Ricarte et al. 2019; Hasinger 2020; Cappelluti et al. 2022; Kashlinsky et al. 2025) and direct collapse black holes (DCBHs) (Yue et al. 2013; Ricarte et al. 2019) are proposed to have observable contributions to the CIB-CXB cross-power spectrum, specifically at large angular scales given that DCBHs would be highly biased with respect to the underlying dark matter distribution.

Using angular Fourier analysis has proved thus far to be a powerful tool for studying the CIB and its coherence with the soft CXB. This technique can provide constraints on the number density of sources producing these unresolved backgrounds and how they are spatially distributed. In particular, statistically significant measurements of the CIB auto- and CIB-CXB cross-power signals as a function of redshift hold important information regarding how SFGs and AGNs evolve in their large-scale structures (Powell et al. 2020; Paque-reau et al. 2025).

The first two years of *JWST* operations showed that at $z > 5$ a larger than expected population of overmassive SMBHs live in primordial galaxies that seem to be more massive than expected (Natarajan et al. 2024). However, as of today, there have been few serendipitous detections of X-rays from galaxies at $z > 6$ (Bogdán et al. 2024). This hinders our ability to place constraints on the first AGNs that populated the Universe in the first hundreds of millions of years after the Big Bang.

In this paper, we leverage the exquisite wide-field photometric survey of the COSMOS-Web field (Casey et al. 2023) to study the coherence between the resolved CIB and the unresolved *Chandra* COSMOS-Legacy CXB fluctuations. With the sources contributing to the resolved CIB, we can recreate the diffuse CIB as observed with *Spitzer* surveys by placing sources on the COSMOS-Web field according to their positions as if they were unresolved. This paper is organized as follows. We describe the data employed and outline the computations of the auto- and cross-power spectra in §2. In §3, we present our analysis of the angular power spectra followed by a discussion §4 where we model the

computed angular power spectra. Finally, we summarize our results in §5.

2. DATASET AND METHODOLOGY

2.1. *Chandra*

We use CXB fluctuation maps in the [0.5-2] keV band constructed and analyzed in Li et al. (2018). This data was taken as part of the COSMOS-Legacy survey with a 1.5 deg^2 area and total observing time of 4.6 Ms (Civano et al. 2016). Observations are recorded by arrival time and placed into A and B images, where the first image is for even events and the second is for odd ones. From these images, a mosaic signal map ($A + B$) and noise map ($A - B$) are created. Because the maps have the same exposure time, the only difference in the A and B images will be instrumental effects contributing to the noise of our computations.

Additionally, resolved X-ray sources detected in the field (Civano et al. 2016) are masked using circular masks with radii of $7''$. This method removes over 90% of the source brightness when factoring off-axis PSF degradation and mosaicing, with the remaining flux having no significant contribution to the cross-power spectra computed in Li et al. (2018). Furthermore, extended emission was masked using the maps of Finoguenov et al. (2007). For further information regarding the data reduction and masking, see Li et al. (2018) as maps were directly provided by the authors.

2.2. *COSMOS-Web CIB Map-Making*

In this study, we use the **SourceExtractor++** (SE++, Bertin et al. 2020) photometric catalog of sources in the COSMOS-Web field, a contiguous 0.54 deg^2 NIRCcam imaging survey (Casey et al. 2023). Imaging is done in both the NIRCcam filters F115W, F150W, F277W, and F444W and the MIRI filter F770W (although the latter is only done in 0.19 deg^2). The catalog is developed by extracting photometry using SE++: a χ^2 -image is created by co-adding the four maps (for each NIRCcam filter) and the source detection is performed on the image. Detections are then modeled with a double Sérsic profile and the best-fit model is PSF-matched with the NIRCcam and MIRI maps (Sersic 1968). From the PSF-matching, photometric data for each source in the different maps are obtained. The exact procedures used in constructing the COSMOS-Web catalog(s) can be found in Shuntov et al. (in prep). We simulate CIB maps in the F277W and F444W filters and focus our analysis on the latter.

2.2.1. *CIB Map Production*

Sources with [F277W] & [F444W] > 25 are placed on the sky according to their positions as point sources.

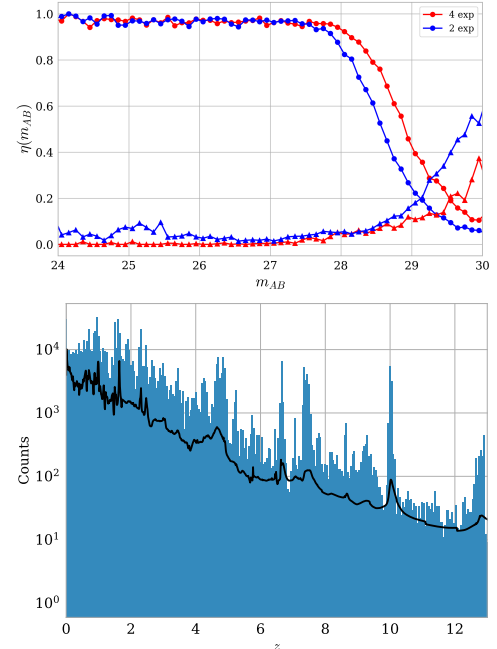


Figure 1. Top: The selection function obtained with the deeper PRIMER survey in the COSMOS field. The different colors signify the completeness for regions of COSMOS-Web with either 2 (blue) or 4 (red) exposures. The circles correspond to the completeness and the triangles to the contamination. Bottom: Best-fit redshift distribution of sources in the COSMOS-Web catalog (blue) and overplotted is the summed z -PDF for all sources (black).

The lower threshold of $m_{AB} = 25$ was chosen so that our CIB maps are only populated by discrete sources which were unresolved by *Spitzer* (see e.g. Kashlinsky et al. 2012, see §3.1). We also place an upper m_{AB} cutoff of 29 which mitigates errors due to contamination (see Fig. 1). The flux density (typically f_ν , but we will use F) is computed for each “point source” assuming a surface area of $0.98'' \times 0.98''$, the same pixel scale as in the CXB fluctuation maps. To account for incompleteness, the flux of each source was weighted by its corresponding selection function $\eta(m_{AB})$.

The selection function (or completeness) of the SE++ catalog is computed using PRIMER (GO #1837), a much deeper survey in the COSMOS and UDS fields (Casey et al. (2023); see Shuntov et al. (in prep.) for further details). Direct measurements of COSMOS-Web sources are compared to those in PRIMER (Dunlop et al. 2021), allowing for a robust assessment of the completeness as a function of magnitude. As discussed in more detail in Casey et al. (2023), COSMOS-Web has a variable depth that changes with the number of exposures N . Of the 0.54 deg^2 area, $\sim 50.8\%$ of it has $N = 2$ and $\sim 47.0\%$ has $N = 4$ (see Fig.

1). Because of the non-uniform sensitivity of the field, a striping effect becomes evident which introduces artificial fluctuations in the subsequent auto- and cross-power spectra. More specifically, an artificial spike in the CIB fluctuations occurs at $\sim 200''$. This effect is mitigated by flattening the $N = 4$ sources according to the $N = 2$ selection function. For the sources with $N = 2$, sources are separated into m_{AB} bins Δm_{AB} where the number of sources in each bin is $n_{N=2}$, which is multiplied by the ratio of the coverage areas ($A_{N=4}/A_{N=2}$). Once this term $n_{N=2}(A_{N=4}/A_{N=2})$ is computed, sources with $N = 4$ are randomly removed until $n_{N=4} = n_{N=2}(A_{N=4}/A_{N=2})$. 1000 iterations of this procedure are performed with negligible differences. Once this procedure is applied, all sources are weighted with the $N = 2$ selection function. Prior to flat fielding, the mean flux of the $N = 2$ and $N = 4$ sources was 6.1978×10^{-11} nW/m² and 5.4566×10^{-11} nW m⁻² respectively. When applying the flat-fielding technique, the $N = 4$ mean flux becomes 6.1955×10^{-11} nW m⁻² and the subsequent power spectra is without the artificial peaks introduced by the striping.

After correcting each source for incompleteness, three maps are created by dividing the catalog into three photometric redshift (photo- z) bins $\Delta z = [0 - 3]$, $[3 - 6]$, and $[6 - 13]$ (see Fig. 1). We do this following the outlined procedure in Allevato et al. (2016) and Powell et al. (2020). The photometric redshift probability distribution function (z -PDF) of each source is computed using the *Le Phare* software (Ilbert et al. 2006; Arnouts et al. 1999). For more detailed information regarding the fitting method, see Shuntov et al. (in prep). The flux of each source is weighted by the z -PDF in each redshift bin and then placed in the respective CIB map. That is, the flux of each source in a given bin is $F(\Delta z) = \int_{z_1}^{z_2} p(z) dz \cdot F$ where the subscripts 1 and 2 are for the lower and upper bounds of each bin respectively. Essentially, the flux is “spread” into each of the different redshift bins. We also analyzed a combined CIB map made of sources from $z = 0$ and $z = 13$ using the same flux-weighting method. In total, there are eight different artificial CIB maps created for each Δz and NIRC*am* filter ($[0 - 3, 3 - 6, 6 - 13, 0 - 13] \times [\text{F277W}, \text{F444W}]$).

Furthermore, sources flagged in the COSMOS-Web catalog are masked. This includes sources that are present in the *JWST* and *Hyper Suprime-Cam* (or *HSC*) star masks, in addition to sources that have *Chandra* counterparts. Additionally, sources with contaminated photo- z measurements (Shuntov et al. in prep) are removed. Finally, all masked sources are combined in one map, which is joined with the *Chandra* mask (Li

et al. 2018), resulting in one singular mask applied to all CIB and CXB maps.

2.3. Fourier Analysis of the CIB and CXB Fluctuations

The CIB and CXB flux maps are then converted into fluctuation maps with: $\delta F(\mathbf{x}) = F(\mathbf{x}) - \langle F \rangle$, where $F(\mathbf{x})$ is the flux at a given pixel and $\langle F \rangle$ is the average flux. The Fourier transform of these fluctuations, $\Delta(\mathbf{q}) = \int \delta F e^{-i\mathbf{x} \cdot \mathbf{q}} d^2x$, is used to compute the angular auto-power spectrum $P(\mathbf{q}) = \langle |\Delta(\mathbf{q})|^2 \rangle$. The goal of our study is to analyze the cross-power spectrum and coherence of the CIB and CXB up to ~ 0.5 deg scale. To avoid masking effects on the auto- and cross-power spectra we require a significant fraction of unmasked pixels (Kashlinsky et al. 2005, 2012). Here we obtained an unmasked fraction of $\sim 65\%$ hence Fourier analysis can be used instead of two-point statistics (Kashlinsky et al. 2005).

Following Cappelluti et al. (2013, 2017b); Li et al. (2018), the auto-power of the $A - B$ map is subtracted from the auto-power of the $A + B$ map to retrieve the clean auto-power spectrum of the CXB. Furthermore, we compute the cross-power spectra of the CIB and CXB expressed as $P_{IR,X}(\mathbf{q}) = \langle \Delta_{IR}(\mathbf{q}) \Delta_X^*(\mathbf{q}) \rangle$. This is done by cross-correlating the CIB fluctuation maps with the X-ray $\delta F_{A+B}(\mathbf{x})$ and $\delta F_{A-B}(\mathbf{x})$ maps separately and then taking the difference to construct the clean CIB-CXB cross-power spectrum. In total, there are eight CIB auto-power spectra (for $[0 - 3, 3 - 6, 6 - 13, 0 - 13] \times [\text{F277W}, \text{F444W}]$) and eight corresponding cross-power spectra, all with the same mask applied.

For both the auto- and cross-power spectra we define the uncertainty at a given angular scale $\frac{2\pi}{q}$ using Poissonian estimators with $\frac{P_{IR}}{\sqrt{0.5N_q}}$ and $\sqrt{\frac{P_{IR}P_X}{N_q}}$ for the auto- and cross-power spectra respectively. In the previous expressions, $0.5N_q$ is defined as the number of independent Fourier elements at a given q . In this work we also quantify the broadband auto- and cross-power signals defined as

$$\langle P_{IR} \rangle = \frac{\sum \sigma_{IR}(q) \cdot P_{IR}(q)}{\sum \sigma_{IR}(q)} \quad (1)$$

and

$$\langle P_{IR,X} \rangle = \frac{\sum \sigma_{IR,X}(q) \cdot P_{IR,X}(q)}{\sum \sigma_{IR,X}(q)} \quad (2)$$

where σ_{IR} and $\sigma_{IR,X}$ are the uncertainties in the auto- and cross-power measurements.

The relative contribution of the emission of one background to the other can be parameterized by a coherence

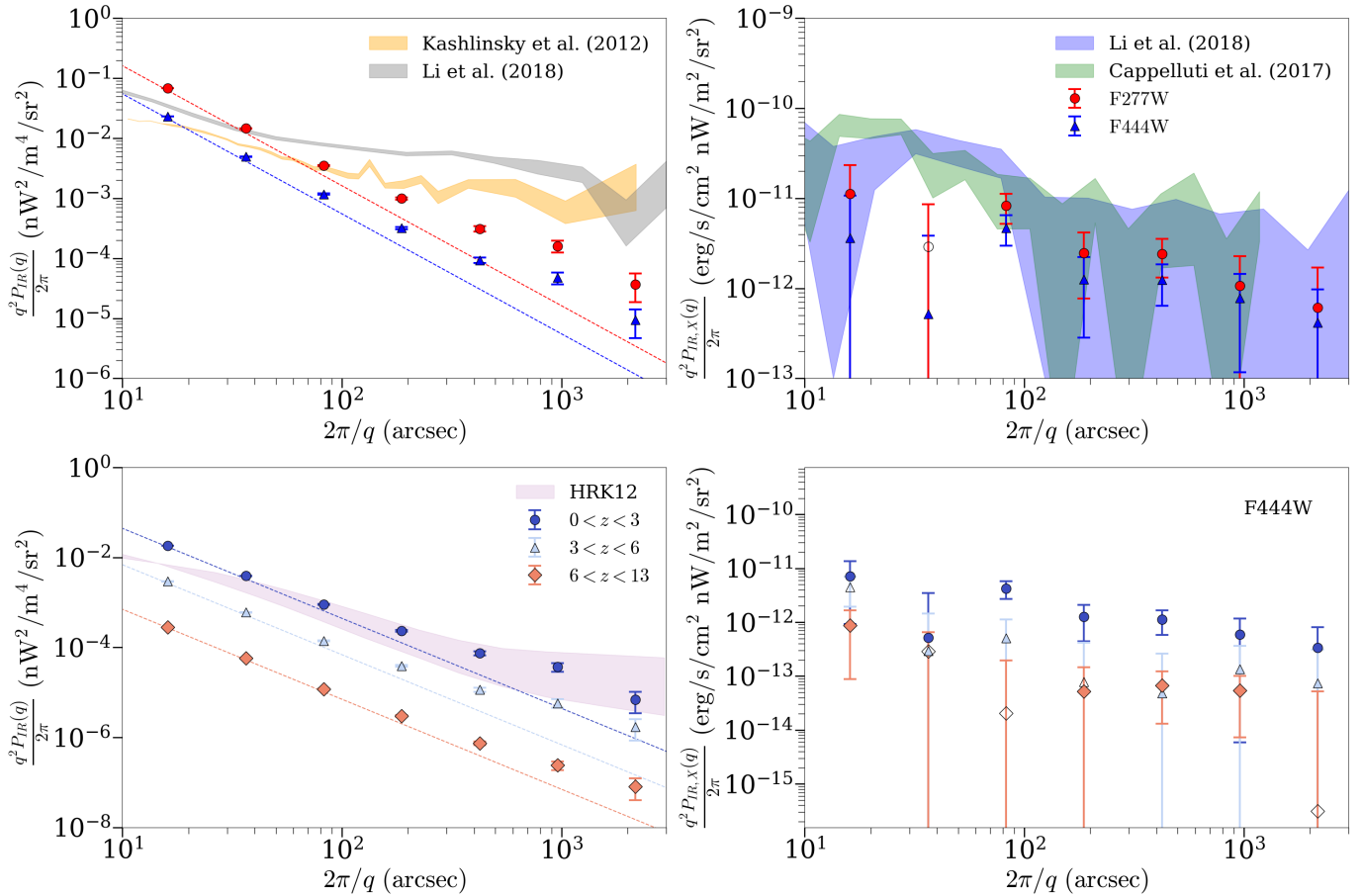


Figure 2. *Upper Left:* Auto-Power spectra of the CIB fluctuations for F277W and F444W CIB fluctuation maps, denoted with the red circles and blue triangles respectively. The dashed lines indicate the shot noise levels computed directly from the COSMOS-Web source counts. The filled-in orange and gray regions correspond to the same computation done in [Kashlinsky et al. \(2012\)](#) ($m_{lim} \sim 25$) and [Li et al. \(2018\)](#) ($m_{lim} = 24.2$) respectively, both of which use measurements of the CIB at $4.5 \mu\text{m}$. *Upper Right:* Cross-Power spectra of the F277W and F444W and the [0.5-2] keV CXB. The filled-in green and blue regions correspond to the same computations done in [Cappelluti et al. \(2017b\)](#) and [Li et al. \(2018\)](#), respectively. *Bottom Left:* Auto-Power spectra for each redshift bin of the F444W map, with the circles, triangles, and diamonds corresponding to the $\Delta z = [0-3], [3-6], [6-13]$ bins respectively. The dashed lines are used again to indicate the shot noise levels computed directly from the source counts. Overplotted in purple is the auto-power spectrum of known populations at $z \leq 6$ ([Helgason et al. 2012](#)). *Bottom Right:* Cross-Power spectra for each redshift bin of the F444W map. Errors are reported at the 1σ confidence level.

term \mathcal{C} , expressed as

$$\mathcal{C}(q) = \frac{P_{IR,X}^2}{P_X P_{IR}} \quad (3)$$

This quantity indicates how much of one signal (either the CXB or CIB auto-power) is present in the other. Looking at the two extremes, $\mathcal{C} = 0$ points to the scenario that there is no contribution from one background to the other, and alternatively $\mathcal{C} = 1$ means that all of the signal from one background contributes to the other.

3. RESULTS

3.1. CIB Auto-Power Spectra

In Fig. 2 we present the CIB auto-power spectra computed in the broad ($[0-13]$) and narrow ($[0-3, 3-6,$

$6-13]$) redshift bins. In the broad Δz bin, upon initial inspection a flat (shot) noise component at low angular scales and an increasing (clustering) component at larger angular scales is visible for both the F277W and F444W maps. The shot noise is estimated as the auto-power signal measured at $\sim 1''$ given a $\Delta \log(q)$ of 0.35, yielding a value of $6.076 \pm 0.006 \times 10^{-11}$ and $2.067 \pm 0.002 \times 10^{-11} \text{ nW}^2 \text{ m}^{-4} \text{ sr}^{-1}$, for the F277W and F444W bands respectively. We can compare these values to calculations of the shot noise using the COSMOS-Web source catalogs with the following expression

$$P_{IR}^{\text{SN}} = \int_{m_{lim}}^{\infty} f^2(m_{AB}) \frac{dN}{dm_{AB}} dm_{AB} \quad (4)$$

where $f(m_{AB})$ is the flux and dN/dm_{AB} is the differential number counts per deg^2 . Calculating this term in the $\Delta z = [0 - 13]$ bin results in a value of 6.072×10^{-11} and $2.064 \times 10^{-11} \text{ nW}^2 \text{ m}^{-4} \text{ sr}^{-1}$ for the F277W and F444W bands respectively, consistent with the directly fitted values. This consistency serves as a sanity check for the CIB map creation technique.

The signal-to-noise ratio S/N of the CIB auto-power spectrum in the broad redshift bin for the both the F277W and F444W maps is ~ 11 when sampling angular scales from $\sim 1 - 3000''$. Furthermore, we compute the average auto-power signal $\langle P_{IR} \rangle$ at scales above $100''$ resulting in measurements of 6.01×10^{-10} and $1.57 \times 10^{-10} \text{ nW}^2 \text{ m}^{-4} \text{ sr}^{-1}$ for the F277W and F444W maps respectively. Both values are found at a S/N of ~ 5 , showing a statistically significant signal due to the large-scale spatial distribution of galaxies (both in the linear and non-linear regimes).

Furthermore, we can compare the auto-power spectrum in the F444W filter with the measurements of the unresolved CIB analyzed in Kashlinsky et al. (2012). In their analysis, field-average auto-power spectra were computed from the Ultra-Deep Survey and Extended Groth Strip (UDS and EDS respectively; (Fazio & Seds Team 2011)) to a shot noise level corresponding to $m_{lim} \approx 25$. The UDS and EDS fields are ~ 0.12 and $\sim 0.14 \text{ deg}^2$ respectively. The clustering component at large angular scales is lower than their field-averaged signal (see Fig. 2). The differences found between our results and those from Kashlinsky et al. (2012) could be due to cosmic variance given the smaller area sampled and the completeness of both maps. The discrepancies between the two results may also originate from additional diffuse CIB emission. We compute the integrated auto-power over $100 - 2000''$ using our results and those from Kashlinsky et al. (2012), and we find that the ratio of the two is $\sim 5 - 15\%$. Given that our signal is entirely extragalactic, we can estimate that $\sim 5 - 15\%$ of the clustering signal from Kashlinsky et al. (2012) arises from galaxies below the *Spitzer* flux limit from at least $\Delta z = [0 - 13]$.

The CIB auto-power signals in the redshift bins $\Delta z = [0 - 3]$, $[3 - 6]$, and $[6 - 13]$ for both the F277W and F444W maps are statistically significant at the $\sim 11\sigma$ level (sampling scales $\sim 1 - 3000''$). For the F277W maps, the directly estimated shot noise values are $4.859 \pm 0.005 \times 10^{-11}$, $7.992 \pm 0.007 \times 10^{-12}$, and $4.315 \pm 0.004 \times 10^{-13} \text{ nW}^2 \text{ m}^{-4} \text{ sr}^{-1}$ for the $\Delta z = [0 - 3]$, $[3 - 6]$, and $[6 - 13]$ bins respectively. These values can be compared to the shot noise power computed directly from the source counts, which is 4.864×10^{-11} , 7.964×10^{-12} , and $4.312 \times 10^{-13} \text{ nW}^2 \text{ m}^{-4} \text{ sr}^{-1}$ for each

respective Δz bin. The estimated and directly computed shot noise values for each redshift interval are consistent within 1σ except for the intermediate bin $\Delta z = [3 - 6]$, which differs at the $\sim 4\sigma$ level. For each Δz we compute the average auto-power signal $\langle P_{IR} \rangle$ at scales above $100''$, resulting in values of 4.16×10^{-10} , 9.24×10^{-11} , and $1.72 \times 10^{-12} \text{ nW}^2 \text{ m}^{-4} \text{ sr}^{-1}$, each with a S/N of 4.98, 5.2, and 5.0 respectively.

The previous analysis of the CIB observed in the F277W filter is extended to the F444W maps. The directly estimated shot noise values are $1.659 \pm 0.002 \times 10^{-11}$, $2.584 \pm 0.002 \times 10^{-12}$, and $2.634 \pm 0.002 \times 10^{-13} \text{ nW}^2 \text{ m}^{-4} \text{ sr}^{-1}$ for each respective Δz bin. The shot noise levels computed from the source catalogs for each redshift interval are 1.657×10^{-11} , 2.580×10^{-12} , and $2.639 \times 10^{-13} \text{ nW}^2 \text{ m}^{-4} \text{ sr}^{-1}$, which is consistent with the direct estimates within $\sim 1.5\sigma$. For the $\Delta z = [0 - 3]$, $[3 - 6]$, and $[6 - 13]$ maps, the $\langle P_{IR} \rangle$ values above $100''$ are 1.18×10^{-10} , 2.68×10^{-11} , and $1.26 \times 10^{-12} \text{ nW}^2 \text{ m}^{-4} \text{ sr}^{-1}$ respectively. The S/N of each value is 5.0, 5.2, and 5.2 respectively. It is important to note that when transitioning from the broad to narrow Δz bins there is a systematic uncertainty introduced that is $\leq 7\%$, which is found in both the number counts and maps generated (which are done independently).

Furthermore, we can pay attention specifically to the $[0 - 3]$ and $[3 - 6]$ auto-power spectra, and compare our results to the reconstructed auto-power from known galaxies at $z < 6$ computed in Helgason et al. (2012). In their work, they take 233 luminosity functions and fit their evolution with redshift to obtain number counts below the *Spitzer* flux limit. For $m_{lim} = 25$, the corresponding upper and lower limits on the CIB shot noise power is ~ 0.6 and $\sim 3 \times 10^{-11} \text{ nW}^2 \text{ m}^{-4} \text{ sr}^{-1}$ respectively. We thus find that our shot noise level of $1.93 \times 10^{-11} \text{ nW}^2 \text{ m}^{-4} \text{ sr}^{-1}$, computed directly from the COSMOS-Web source counts, is consistent with their results (Helgason et al. 2012). Additionally, we find that the large-scale power computed in this study is within the range of allowed models from Helgason et al. (2012) (see Fig. 2).

3.2. CIB-CXB Cross-Power Spectra

In this study we report cross-power spectra with S/N measurements $> 4\sigma$ at angular scales $1 - 1000''$. We find that the S/N of the cross-power signals in the $\Delta z = [0 - 13]$ interval are ~ 4.8 and 6.2 , corresponding to the F277W and F444W maps, respectively.

The S/N of the narrower Δz cross-power signals are shown in Table 1 for both the F277W $\times [0.5-2]$ keV and F444W $\times [0.5-2]$ keV cross-correlations.

4. DISCUSSION

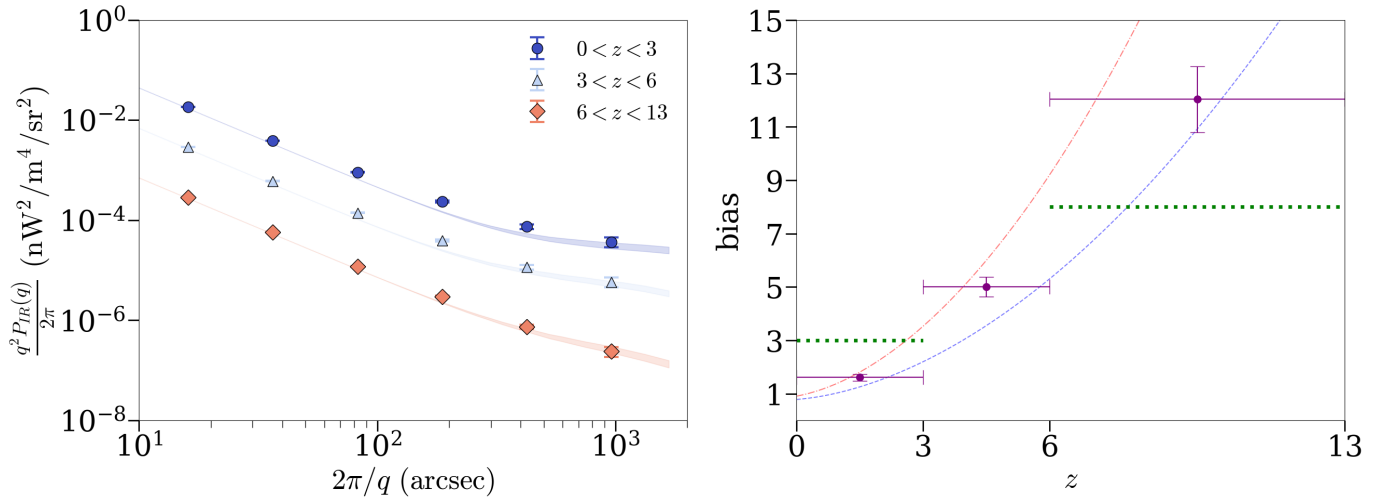


Figure 3. *Left:* Modeled F444W CIB auto-power spectra for each Δz bin. The circles, triangles, and diamonds correspond to the $\Delta z = [0 - 3], [3 - 6], [6 - 13]$ bins respectively. *Right:* Best-fit bias \tilde{b}_{IR} as a function of z . The dashed blue and dash-dotted red lines correspond to the biasing of dark matter halos with masses of $10^{11} M_{\odot} h^{-1}$ and $10^{12} M_{\odot} h^{-1}$ respectively (Sheth et al. 2001). The green dotted lines correspond to the lower limits of the biasing of coherent X-ray sources.

Average Cross-Power Spectra				
Δz	$\langle P_{IR,X} \rangle_{F277W}^a$	S/N_{F277W}	$\langle P_{IR,X} \rangle_{F444W}^a$	S/N_{F444W}
0 - 3	25.2 ± 5.81	4.34	17.2 ± 3.18	5.40
3 - 6	3.95 ± 0.24	1.67	3.73 ± 1.26	2.95
6 - 13	2.48 ± 0.34	7.32	1.47 ± 0.27	5.39
0 - 13	23.8 ± 5.77	4.80	22.5 ± 3.61	6.20

$a \times 10^{-19} \text{ erg/s/cm}^2 \text{ nW/m}^2/\text{sr}$

Table 1. The average cross-power signal is computed in each redshift bin ranging from the angular scales $1 - 1000''$. The top and bottom sections of the table are measurements using the F277W and F444W maps, respectively.

4.1. Modeling the CIB Auto-Power Spectra

Direct knowledge of the populations contributing to the CIB (i.e. source counts) allows us to constrain the large-scale clustering of these populations as a function of redshift. As mentioned previously, the CIB angular power can be written as

$$P_{IR}^{\text{tot}}(q) = P_{IR}^{\text{SN}} + P_{IR}^{\text{Cl}}(q) \quad (5)$$

where the superscripts “SN” and “Cl” denote the shot noise and clustering components respectively. The shot noise component of the CIB auto-power spectra was computed in §3.1, therefore isolating the power due to galaxy clustering. This term can be described by Limber’s equation (Limber 1953)

$$P_{IR}^{\text{Cl}}(q) = \int_{z_{\min}}^{z_{\max}} \frac{H(z)}{cd_c^2(z)} \left[\frac{dF_{CIB}}{dz} \right]^2 P(qd_c^{-1}, z) dz \quad (6)$$

where H is the Hubble factor, d_c is the co-moving distance, dF_{CIB}/dz is the flux production rate of the CIB, and $P(qd_c^{-1}, z)$ is the 3D power spectrum. The flux production rate of the CIB can be written as

$$\frac{dF_{CIB}}{dz} = \int f(m_{AB}) \frac{d^3 N}{dm_{AB} d\Omega dz} dm_{AB}. \quad (7)$$

Furthermore, for our analysis we only consider angular scales $\gtrsim 300''$ as in this regime the galaxy power spectrum is safely within the linear approximation (Helgason et al. 2012). As a result the 3D galaxy power spectrum is defined as

$$P(qd_c^{-1}, z) = b^2 P_{\Lambda\text{CDM}}(k, z) \quad (8)$$

where b is the large-scale bias, or clustering strength of galaxies with respect to dark matter, and $P_{\Lambda\text{CDM}}$ is the 3D power spectrum of dark matter. Essentially, the bias parameter encapsulates the physics of galaxy formation and evolution, including processes impacting and/or driven by star formation and black hole activity (Desjacques et al. 2018; Paquereau et al. 2025). To compute the linear matter power spectrum, we use the cosmology package COLOSSUS (Diemer 2018).

In this analysis the sole parameter we fit is the average biasing of the CIB sources, \tilde{b}_{IR} . In this fit we employ the Python package `emcee`, an affine-invariant ensemble sampler introduced by Foreman-Mackey et al. (2013). We sample parameter-space assuming a flat prior distribution using 5 walkers and 500 steps. The likelihood function $\ln(P)$ is written in the form of

$$\ln(P) = -\frac{1}{2} \chi^2 \quad (9)$$

where

$$\chi^2 = \sum \left(\frac{P_{IR}^{\text{tot}}(q) - P_{IR}^{\text{obs}}(q)}{\sigma_{IR}^{\text{obs}}(q)} \right)^2 \quad (10)$$

where the “tot” superscript indicates the model power spectra while the “obs” superscript indicates the observed power spectra. We confirm that in each redshift interval the MCMC chain converges and is independent of the prior bounds used. The best-fit values of \tilde{b}_{IR} in the $[0 - 3]$, $[3 - 6]$, and $[6 - 13]$ Δz bins are $1.61_{-0.14}^{+0.13}$, $5.01_{-0.39}^{+0.37}$, and $12.04_{-1.28}^{+1.19}$ respectively. Each fit has a reduced χ^2 of 1.44, 0.81, and 0.42 for each redshift interval respectively. The fitted CIB auto-power spectra and associated \tilde{b}_{IR} values can be found in Fig. 3.

4.2. Estimated CXB Flux Production

An in-depth treatment of the CXB in regards to its population characteristics, abundance, and clustering will be the focus of a forthcoming paper. However, we can first estimate the CXB flux production rate as a function of redshift using the auto- and cross-power spectra computed in this study. Here, we first approximate the *coherent* rms CXB fluctuations δF_{CXB} as a function of q in each Δz bin to be

$$\delta F_{CXB}(q) = \sqrt{\frac{q^2}{2\pi} \frac{P_{IR,X}^2(q)}{P_{IR}(q)P_{PSF}(q)}} \quad (11)$$

where we introduce $P_{PSF}(q)$ to be the power due to the *Chandra* beam, taken to be Eq. 11 of Cappelluti et al. (2012b). We use Monte Carlo sampling with the associated errors of the auto- and cross-power spectra (with a total of 10000 samples) to compute the mean flux of the CXB. This procedure is done in each Δz bin. The resulting CXB flux $\langle F_{CXB} \rangle$ in each interval is $9.68_{-4.15}^{+5.73}$, $8.72_{-3.83}^{+5.54}$, and $7.99_{-3.52}^{+5.24} \times 10^{-14}$ erg/s/cm²/deg² respectively. We find the total *coherent* CXB flux $\langle F_{CXB} \rangle$ to be $2.64_{-0.67}^{+0.52} \times 10^{-13}$ erg/s/cm²/deg², which is within the upper limit of the total unresolved CXB flux measured in Cappelluti et al. (2017a).

In Figure 4 we show the cumulative $[0.5-2]$ keV CXB flux production as a function of redshift, compared with the flux derived by Cappelluti et al. (2017a) in the COSMOS-Legacy Survey for sources below IR magnitude limits similar to those applied in our mask. Cappelluti et al. (2017a) reported an unresolved CXB surface brightness of $9.7_{-1.8}^{+1.6} \times 10^{-13}$ erg/s/cm²/deg², whereas we find a value of $2.63_{-0.67}^{+0.52}$ erg/s/cm²/deg², corresponding to $27_{-10}^{+13}\%$ of their unresolved CXB. These results show that approximately 94% of the CXB has been resolved. When accounting for systematic uncertainties in the total CXB measurements, our findings are consistent within 2σ of fully resolving the extragalactic $[0.5-2]$ keV CXB.

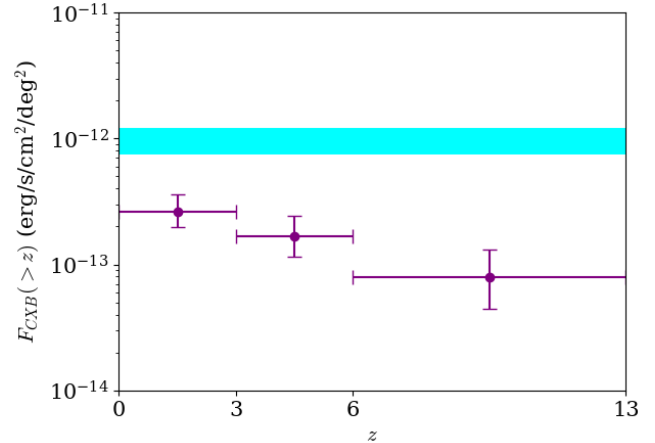


Figure 4. Estimated Cumulative flux contribution of the CXB as a function of redshift. The cyan bar at 0.97×10^{-12} erg/s/cm²/deg² is the upper limit placed on the unresolved CXB in Cappelluti et al. (2017a). The flux contribution of the CXB gets progressively fainter as a function of redshift as expected (Helgason et al. 2014; Cappelluti et al. 2017a), albeit with a weak decline. Errors are reported at the 1σ confidence level.

Without fitting the CIB-CXB cross-power, we can still estimate lower limits on the biasing of X-ray sources, \tilde{b}_X . This is done by using the best-fit \tilde{b}_{IR} , in addition to the derived flux production rates of the CIB and CXB. Then using the following equation

$$P_{IR,X}^{\text{Cl}}(q) = \int_{z_{\text{min}}}^{z_{\text{max}}} \frac{H(z)}{cd_c^2(z)} \frac{dF_{CIB}}{dz} \times P_{\Lambda\text{CDM}}(qd_c^{-1}, z) dz \quad (12)$$

a rough estimate for \tilde{b}_X at $2\pi/q \sim 500''$ is determined. Because of the relatively lower signal in the $\Delta z = [3 - 6]$ bin at larger angular scales, we only perform this estimate in the low- z and high- z bins. For the former, we find a value of ~ 3.27 while in the latter an estimate of ~ 7.80 (see Fig. 3).

4.3. Low- z Populations

The best-fit \tilde{b}_{IR} of $1.61_{-0.14}^{+0.13}$ in the $[0 - 3]$ redshift bin is consistent with previously computed values of the large-scale biasing of SFGs (Coil et al. 2017; Hale et al. 2018). Using the bias prescription from Sheth et al. (2001), this best-fit value corresponds to a characteristic halo mass M_h of $\sim 10^{11} M_\odot h^{-1}$, further pointing toward a population of faint SFGs resolved by *JWST*. This is expected given that the majority of the sources in the COSMOS-Web field are SFGs (Shuntov et al. 2024). Additionally, the \tilde{b}_{IR} value discussed here is consistent with the galaxy bias for SFGs computed in the COSMOS-Web field (Paquereau et al. 2025), with their results ranging

from $b \sim 1 - 5$ in the redshift interval $[0 - 3]$, with the spread due to binning galaxies according to their stellar mass M_* . The total z -PDF of our sources peaks near $z \sim 1$, where the bias reported in Paquereau et al. (2025) is ~ 1.5 , bringing our results into even closer agreement. Furthermore, these results are unsurprising given the apparent consistency of these results with the CIB auto-power spectrum modeled by Helgason et al. (2012), which is entirely the result of stellar emission produced mostly within the range $1 \lesssim z \lesssim 3$.

The low- z CIB signal detected in this study has several implications for the $\sim 5\sigma$ cross-power signal reported. It is expected that SFGs (1) dominate the low-flux regime of the X-ray $\log(N)$ - $\log(S)$ and (2) contribute to $\sim 25\%$ of the unresolved CXB anisotropies (Cappelluti et al. 2012b, 2016). As a result, it is entirely possible that the coherence seen at low- z can at least in part be due to SFGs that emit in both the IR and soft X-rays (Helgason et al. 2014).

Additionally, we expect that star-forming populations and AGNs cluster within the same large-scale structures (Helgason et al. 2014), so the CIB-CXB cross-power signal detected may be a reflection of these distinct populations clustered together. The lower limit of \tilde{b}_X at low- z is significantly higher than the biasing of CIB sources, which may support the claim that the cross-power signal is produced by SFGs in the IR and AGNs in the X-ray. As $\tilde{b}_X \sim 3.27$, this corresponds to $M_h \sim 10^{13} M_\odot h^{-1}$, a halo mass regime characteristic of AGN hosts. According to Helgason et al. (2014), between $0 \lesssim z \lesssim 3$ the biasing of AGNs can go as high as $b \sim 4$, which is consistent with our value. Further modeling of the CIB-CXB cross-power signal is needed to shed light on the precise populations contributing to the unresolved soft CXB in this redshift range.

4.4. High- z Populations

The best-fit high- z \tilde{b}_{IR} and $\langle F_{CXB} \rangle$ values of $12.03^{+1.19}_{-1.28}$ and $7.99^{+5.24}_{-3.52} \times 10^{-14}$ erg s $^{-1}$ cm $^{-2}$ deg $^{-2}$ respectively hold several implications for the sources contributing to the CIB and CIB-CXB angular power spectra. The \tilde{b}_{IR} derived in this redshift interval is within the $\sim 7 - 15$ range put forth by Paquereau et al. (2025), and corresponds to a halo mass of $\sim 10^{11} M_\odot h^{-1}$. According to the results of Shuntov et al. (2024), this halo mass corresponds to galaxies with stellar masses as high as $\sim 5 \times 10^{10} M_\odot$. It is entirely possible that these early, massive galaxies were clustered in the same large-scale environments as early AGNs. The lower limit we place on the \tilde{b}_X parameter at high- z of ~ 7.8 (corresponding to $M_h \sim 10^{10} M_\odot h^{-1}$) is consistent with previously modeled high-mass SMBH seeds (Ricarte et al. 2019),

suggesting that these sources may be massively accreting SMBHs. Further on this note, it has been proposed that these high- z AGNs can boost the CIB-CXB cross-power signal (Ricarte et al. 2019; Cappelluti et al. 2022), an interpretation that can be tested with the $\sim 5\sigma$ signal reported in this work. If we assume that the CXB flux at $z > 6$ is primarily powered by accretion onto SMBHs (Cappelluti et al. 2022), we can invoke Soltan's Argument (Soltan 1982) to estimate the BH accreted mass density ρ_{acc} as outlined in Salvaterra et al. (2012)

$$\rho_{acc}(z) = 4\pi \frac{1 - \epsilon}{\epsilon c^3} \frac{E_0 J_{E_0}}{f_X (1 - \alpha)} \frac{\alpha + \gamma + \frac{3}{2}}{\gamma + \frac{3}{2}} (1 + z)^\alpha \times \left[\left(\frac{E_M}{E_0} \right)^{1-\alpha} - \left(\frac{E_m}{E_0} \right)^{1-\alpha} \right] \quad (13)$$

where ϵ , f_X , α , γ are the mass-accretion conversion efficiency, bolometric correction constant, AGN spectrum slope, and a constant characterizing the redshift evolution of the comoving specific emissivity respectively. E_0 is the background energy and J_{E_0} is the emissivity observed at E_0 , and E_m and E_M are the lower and upper bounds (respectively) of the X-ray band evaluated. We use the bolometric correction constant at $z = 6$ derived in Ricarte et al. (2019) and assume that $(\alpha + \gamma + \frac{3}{2})/(\gamma + \frac{3}{2}) \simeq 1$. Additionally, we assume ϵ to be 0.1. Plugging in each of these values and the derived CXB flux at $z > 6$, we estimate that $\rho_{acc} \approx 10^{5.15} M_\odot \text{Mpc}^{-3}$. Our result is consistent with the upper limits put forth in Cappelluti et al. (2017a). It is also important to include that our ρ_{acc} at $z = 6$ is only slightly under local estimates according to Hopkins et al. (2007) and Shankar et al. (2009) which are $\log \rho_{acc}(z = 0) \sim 5.5 - 5.7$. This is due in-part by the assumed bolometric correction from Ricarte et al. (2019) and the order-of-magnitude CXB flux estimate here.

Another interesting estimate is the number density of sources producing the level of Cosmic X-ray Background (CXB) responsible for the observed cross-power. By assuming, for simplicity, that the X-ray source counts in the high-redshift bin (i.e., $\Delta z = [6 - 13]$) behave in a Euclidean manner, the CXB production at redshift z can be expressed as

$$F_{CXB}(z) = \int_{S_{lim}}^{\infty} S \frac{dN}{dS}(z) dS \quad (14)$$

where the differential number counts can be written as

$$\frac{dN}{dS}(z) \propto k \left(\frac{S}{S_0} \right)^{-2.5}. \quad (15)$$

Here, k is the normalization and $S_0 = 4.2 \times 10^{-18}$ erg s $^{-1}$ cm $^{-2}$ (the typical flux limit of a moderately deep AXIS

survey, Reynolds et al. 2023). With this assumption, we find a source density on the order of 500–700 deg⁻², consistent with the predictions of the semi-analytic model of Ricarte & Natarajan (2018). Although the number density can be constrained, we cannot disentangle their SMBH seeding models.

Future work will leverage the robust data obtained in the COSMOS-Web field, including a catalog of star formation rates (SFRs) and stellar masses (M_*) (priv. comm.) computed using the SED fitting code CIGALE (Boquien et al. 2019). These quantities alongside others will be used in conjunction with the artificial map creation method invoked in this work to shed light on the contributions of SFGs and AGNs to the observed CIB-CXB cross-power signal at high- z .

5. SUMMARY

In this study, we utilize *JWST* observations of resolved sources in the F277W and F444W bands from the COSMOS-Web survey (Casey et al. 2023) to create CIB fluctuation maps. Sources brighter than the magnitude limit $m_{AB} = 25$ (the *Spitzer* limit) were masked. The auto-power spectra of each map were computed and cross-correlated with the unresolved [0.5–2] keV CXB as observed by *Chandra*. Our main results can be summarized as the following:

1. The CIB-CXB cross-power signal measured with sources below the *Spitzer* flux limit is statistically significant with a S/N of 4.80 and 6.20 at angular scales 1 – 1000'', for the F277W and F444W CIB fluctuations respectively. The cross-power spectrum at F444W is consistent with the measured spectra from Cappelluti et al. (2013) and Li et al. (2018), demonstrating that the previously detected cross-power can be explained by galaxy populations revealed by *JWST*. This significance allows us to conclude that sources resolved by *JWST* emit soft X-rays and are clustered on larger spatial scales. The significance of this cross-power spectrum in different Δz ranges has also been computed and notably we find for the first time evidence of significant emission of X-rays among the newly discovered population of *JWST* $z > 6$ galaxies.
2. We estimate the lower limit of the unresolved [0.5–2] keV CXB flux in the redshift range $0 < z < 13$ to be $2.64_{-0.67}^{+0.52} \times 10^{-13}$ erg/s/cm²/deg². If the CXB flux at $z > 6$ is produced entirely by AGNs, this corresponds to a black hole accreted mass density of $\rho_{acc} \approx 10^{5.15} M_\odot \text{Mpc}^{-3}$. These results are consistent with the findings of (Cappelluti et al.

2017a). In the low- and high- z intervals probed we place lower limits on the biasing of these X-ray sources to be ~ 3.27 and 7.80 respectively, corresponding to halo masses of 10^{13} and $10^{10} M_\odot h^{-1}$.

3. We resolve $27_{-10}^{+13}\%$ of the unresolved CXB measured by Cappelluti et al. (2017a). This brings the resolved fraction of the CXB to at least $\sim 94\%$. The remaining fraction of the unresolved CXB, if any, can be attributed to diffuse X-ray sources and/or systematic uncertainties in the actual CXB flux. At $6 < z < 13$ the CXB production rate measured here roughly corresponds to a source surface density of 500–700 deg⁻².
4. We find a statistically significant excess in the CIB auto-power spectrum of maps in both the F277W and F444W maps. For the latter, we find that the auto-power spectrum is significantly lower than the 4.5 μm CIB auto-power spectrum computed in Kashlinsky et al. (2012) and Li et al. (2018), leaving their detected clustering component still unexplained by known galaxy populations (Helgason et al. 2012).
5. The CIB power spectrum was evaluated at $\Delta z = [0 - 3], [3 - 6], [6 - 13],$ and $[0 - 13]$. We find a clustering excess at large scales with fluctuations that drop as redshift increases. Specifically, with the auto-power spectra in the $[0 - 3]$ and $[3 - 6]$ bins, we find close similarity with the reconstructed CIB fluctuations derived in Helgason et al. (2012). Each auto-power spectrum is fitted using MCMC methods to obtain large-scale biases of $1.59_{-0.13}^{+0.12}$, $5.21_{-0.39}^{+0.36}$, and $12.29_{-1.26}^{+1.15}$ for each respective Δz bin. These values correspond to halo masses on the order of $10^{11} M_\odot h^{-1}$.

The unprecedented quality data gathered in the COSMOS-Web field provides a powerful boost to the Fourier analysis of the very faint CIB fluctuations as a function of source brightness and redshift. Future work will make use of derived source properties in order to further constrain the populations behind the CIB-CXB cross-power spectrum at all spatial scales, quantifying the abundance and clustering of SFGs and AGNs. This will have important implications for constraining SMBH seeding mechanisms and populations responsible for reionization. Finally, this study shows that, although individually undetectable, high- z AGN contribute to the CXB. Consequently, future, more powerful X-ray telescopes, such as AXIS (Reynolds et al. 2023), will resolve

these sources and further enhance our understanding of faint, high- z accreting SMBHs.

1 N.C., A.K. and J.S. acknowledge JWST-AR-03303.002-
 2 A and Chandra grant AR3-24008X. N.C., A.K. and J.S.
 3 acknowledge the University of Miami for partially sup-
 4 porting this investigation. A.K. acknowledges insightful
 5 discussions with Alberto Magaraggia, Angelo Ricarte,
 6 and Richard G. Arendt regarding map-making and X-
 7 ray number counts. All the authors acknowledge the
 8 outstanding job of the Chandra X-ray Observatory and
 9 JWST teams. We kindly acknowledge the COSMOS-
 10 Web team for insightful discussions and support on data
 11 products.

Facilities: JWST, Chandra

Software: astropy (Astropy Collaboration et al. 2013, 2018), Source Extractor (Bertin & Arnouts 1996) COLOSSUS (Diemer 2018), emcee (Foreman-Mackey et al. 2013)

REFERENCES

- Allevato, V., Civano, F., Finoguenov, A., et al. 2016, ApJ, 832, 70, doi: [10.3847/0004-637X/832/1/70](https://doi.org/10.3847/0004-637X/832/1/70)
- Arnouts, S., Cristiani, S., Moscardini, L., et al. 1999, MNRAS, 310, 540, doi: [10.1046/j.1365-8711.1999.02978.x](https://doi.org/10.1046/j.1365-8711.1999.02978.x)
- Astropy Collaboration, Robitaille, T. P., Tollerud, E. J., et al. 2013, A&A, 558, A33, doi: [10.1051/0004-6361/201322068](https://doi.org/10.1051/0004-6361/201322068)
- Astropy Collaboration, Price-Whelan, A. M., Sipőcz, B. M., et al. 2018, AJ, 156, 123, doi: [10.3847/1538-3881/aabc4f](https://doi.org/10.3847/1538-3881/aabc4f)
- Bertin, E., & Arnouts, S. 1996, A&AS, 117, 393, doi: [10.1051/aas:1996164](https://doi.org/10.1051/aas:1996164)
- Bertin, E., Schefer, M., Apostolakis, N., et al. 2020, in Astronomical Society of the Pacific Conference Series, Vol. 527, Astronomical Data Analysis Software and Systems XXIX, ed. R. Pizzo, E. R. Deul, J. D. Mol, J. de Plaa, & H. Verkouter, 461
- Bogdán, Á., Goulding, A. D., Natarajan, P., et al. 2024, Nature Astronomy, 8, 126, doi: [10.1038/s41550-023-02111-9](https://doi.org/10.1038/s41550-023-02111-9)
- Boquien, M., Burgarella, D., Roehly, Y., et al. 2019, A&A, 622, A103, doi: [10.1051/0004-6361/201834156](https://doi.org/10.1051/0004-6361/201834156)
- Cappelluti, N., Hasinger, G., & Natarajan, P. 2022, ApJ, 926, 205, doi: [10.3847/1538-4357/ac332d](https://doi.org/10.3847/1538-4357/ac332d)
- Cappelluti, N., Ranalli, P., Roncarelli, M., et al. 2012a, MNRAS, 427, 651, doi: [10.1111/j.1365-2966.2012.21867.x](https://doi.org/10.1111/j.1365-2966.2012.21867.x)
- . 2012b, MNRAS, 427, 651, doi: [10.1111/j.1365-2966.2012.21867.x](https://doi.org/10.1111/j.1365-2966.2012.21867.x)
- Cappelluti, N., Kashlinsky, A., Arendt, R. G., et al. 2013, ApJ, 769, 68, doi: [10.1088/0004-637X/769/1/68](https://doi.org/10.1088/0004-637X/769/1/68)
- Cappelluti, N., Comastri, A., Fontana, A., et al. 2016, ApJ, 823, 95, doi: [10.3847/0004-637X/823/2/95](https://doi.org/10.3847/0004-637X/823/2/95)
- Cappelluti, N., Li, Y., Ricarte, A., et al. 2017a, ApJ, 837, 19, doi: [10.3847/1538-4357/aa5ea4](https://doi.org/10.3847/1538-4357/aa5ea4)
- Cappelluti, N., Arendt, R., Kashlinsky, A., et al. 2017b, ApJL, 847, L11, doi: [10.3847/2041-8213/aa8acd](https://doi.org/10.3847/2041-8213/aa8acd)
- Casey, C. M., Kartaltepe, J. S., Drakos, N. E., et al. 2023, ApJ, 954, 31, doi: [10.3847/1538-4357/acc2bc](https://doi.org/10.3847/1538-4357/acc2bc)
- Civano, F., Marchesi, S., Comastri, A., et al. 2016, ApJ, 819, 62, doi: [10.3847/0004-637X/819/1/62](https://doi.org/10.3847/0004-637X/819/1/62)
- Coil, A. L., Mendez, A. J., Eisenstein, D. J., & Moustakas, J. 2017, ApJ, 838, 87, doi: [10.3847/1538-4357/aa63ec](https://doi.org/10.3847/1538-4357/aa63ec)
- Cooray, A., Smidt, J., de Bernardis, F., et al. 2012, Nature, 490, 514, doi: [10.1038/nature11474](https://doi.org/10.1038/nature11474)
- Desjacques, V., Jeong, D., & Schmidt, F. 2018, PhR, 733, 1, doi: [10.1016/j.physrep.2017.12.002](https://doi.org/10.1016/j.physrep.2017.12.002)
- Diemer, B. 2018, ApJS, 239, 35, doi: [10.3847/1538-4365/aace8c](https://doi.org/10.3847/1538-4365/aace8c)
- Dunlop, J. S., Abraham, R. G., Ashby, M. L. N., et al. 2021, PRIMER: Public Release IMAGING for Extragalactic Research, JWST Proposal. Cycle 1, ID. #1837
- Fazio, G. G., & Seds Team. 2011, in Astronomical Society of the Pacific Conference Series, Vol. 446, Galaxy Evolution: Infrared to Millimeter Wavelength Perspective, ed. W. Wang, J. Lu, Z. Luo, Z. Yang, H. Hua, & Z. Chen, 347

- Finoguenov, A., Guzzo, L., Hasinger, G., et al. 2007, *ApJS*, 172, 182, doi: [10.1086/516577](https://doi.org/10.1086/516577)
- Foreman-Mackey, D., Hogg, D. W., Lang, D., & Goodman, J. 2013, *PASP*, 125, 306, doi: [10.1086/670067](https://doi.org/10.1086/670067)
- Giacconi, R., Gursky, H., Paolini, F. R., & Rossi, B. B. 1962, *PhRvL*, 9, 439, doi: [10.1103/PhysRevLett.9.439](https://doi.org/10.1103/PhysRevLett.9.439)
- Hale, C. L., Jarvis, M. J., Delvecchio, I., et al. 2018, *MNRAS*, 474, 4133, doi: [10.1093/mnras/stx2954](https://doi.org/10.1093/mnras/stx2954)
- Hasinger, G. 2020, *JCAP*, 2020, 022, doi: [10.1088/1475-7516/2020/07/022](https://doi.org/10.1088/1475-7516/2020/07/022)
- Helgason, K., Cappelluti, N., Hasinger, G., Kashlinsky, A., & Ricotti, M. 2014, *ApJ*, 785, 38, doi: [10.1088/0004-637X/785/1/38](https://doi.org/10.1088/0004-637X/785/1/38)
- Helgason, K., Ricotti, M., & Kashlinsky, A. 2012, *ApJ*, 752, 113, doi: [10.1088/0004-637X/752/2/113](https://doi.org/10.1088/0004-637X/752/2/113)
- Hickox, R. C., & Markevitch, M. 2007, *ApJL*, 661, L117, doi: [10.1086/519003](https://doi.org/10.1086/519003)
- Hopkins, P. F., Richards, G. T., & Hernquist, L. 2007, *ApJ*, 654, 731, doi: [10.1086/509629](https://doi.org/10.1086/509629)
- Ilbert, O., Arnouts, S., McCracken, H. J., et al. 2006, *A&A*, 457, 841, doi: [10.1051/0004-6361:20065138](https://doi.org/10.1051/0004-6361:20065138)
- Kashlinsky, A. 2016, *ApJL*, 823, L25, doi: [10.3847/2041-8205/823/2/L25](https://doi.org/10.3847/2041-8205/823/2/L25)
- Kashlinsky, A., Arendt, R. G., Ashby, M. L. N., et al. 2012, *ApJ*, 753, 63, doi: [10.1088/0004-637X/753/1/63](https://doi.org/10.1088/0004-637X/753/1/63)
- Kashlinsky, A., Arendt, R. G., Ashby, M. L. N., Kruk, J., & Odegard, N. 2025, *The Astrophysical Journal Letters*, 980, L12, doi: [10.3847/2041-8213/adad5e](https://doi.org/10.3847/2041-8213/adad5e)
- Kashlinsky, A., Arendt, R. G., Atrio-Barandela, F., et al. 2018, *Rev. Mod. Phys.*, 90, 025006, doi: [10.1103/RevModPhys.90.025006](https://doi.org/10.1103/RevModPhys.90.025006)
- Kashlinsky, A., Arendt, R. G., Mather, J., & Moseley, S. H. 2005, *Nature*, 438, 45, doi: [10.1038/nature04143](https://doi.org/10.1038/nature04143)
- Li, Y., Cappelluti, N., Arendt, R. G., et al. 2018, *ApJ*, 864, 141, doi: [10.3847/1538-4357/aad55a](https://doi.org/10.3847/1538-4357/aad55a)
- Limber, D. N. 1953, *ApJ*, 117, 134, doi: [10.1086/145672](https://doi.org/10.1086/145672)
- Matsumoto, T., Seo, H. J., Jeong, W. S., et al. 2011, *ApJ*, 742, 124, doi: [10.1088/0004-637X/742/2/124](https://doi.org/10.1088/0004-637X/742/2/124)
- Mitchell-Wynne, K., Cooray, A., Xue, Y., et al. 2016, *ApJ*, 832, 104, doi: [10.3847/0004-637X/832/2/104](https://doi.org/10.3847/0004-637X/832/2/104)
- Moretti, A., Vattakunnel, S., Tozzi, P., et al. 2012, *A&A*, 548, A87, doi: [10.1051/0004-6361/201219921](https://doi.org/10.1051/0004-6361/201219921)
- Natarajan, P., Pacucci, F., Ricarte, A., et al. 2024, *ApJL*, 960, L1, doi: [10.3847/2041-8213/ad0e76](https://doi.org/10.3847/2041-8213/ad0e76)
- Paquereau, L., Laigle, C., McCracken, H. J., et al. 2025, arXiv e-prints, arXiv:2501.11674, <https://arxiv.org/abs/2501.11674>
- Powell, M. C., Urry, C. M., Cappelluti, N., et al. 2020, *ApJ*, 891, 41, doi: [10.3847/1538-4357/ab6e65](https://doi.org/10.3847/1538-4357/ab6e65)
- Reynolds, C. S., Kara, E. A., Mushotzky, R. F., et al. 2023, in *Society of Photo-Optical Instrumentation Engineers (SPIE) Conference Series*, Vol. 12678, UV, X-Ray, and Gamma-Ray Space Instrumentation for Astronomy XXIII, ed. O. H. Siegmund & K. Hoadley, 126781E, doi: [10.1117/12.2677468](https://doi.org/10.1117/12.2677468)
- Ricarte, A., & Natarajan, P. 2018, *MNRAS*, 474, 1995, doi: [10.1093/mnras/stx2851](https://doi.org/10.1093/mnras/stx2851)
- Ricarte, A., Pacucci, F., Cappelluti, N., & Natarajan, P. 2019, *MNRAS*, 489, 1006, doi: [10.1093/mnras/stz1891](https://doi.org/10.1093/mnras/stz1891)
- Salvaterra, R., Haardt, F., Volonteri, M., & Moretti, A. 2012, *A&A*, 545, L6, doi: [10.1051/0004-6361/201219965](https://doi.org/10.1051/0004-6361/201219965)
- Sersic, J. L. 1968, *Atlas de Galaxias Australes*
- Shankar, F., Weinberg, D. H., & Miralda-Escudé, J. 2009, *ApJ*, 690, 20, doi: [10.1088/0004-637X/690/1/20](https://doi.org/10.1088/0004-637X/690/1/20)
- Sheth, R. K., Mo, H. J., & Tormen, G. 2001, *MNRAS*, 323, 1, doi: [10.1046/j.1365-8711.2001.04006.x](https://doi.org/10.1046/j.1365-8711.2001.04006.x)
- Shuntov, M., Ilbert, O., Toft, S., et al. 2024, arXiv e-prints, arXiv:2410.08290, doi: [10.48550/arXiv.2410.08290](https://doi.org/10.48550/arXiv.2410.08290)
- Soltan, A. 1982, *MNRAS*, 200, 115, doi: [10.1093/mnras/200.1.115](https://doi.org/10.1093/mnras/200.1.115)
- Yue, B., Ferrara, A., Salvaterra, R., & Chen, X. 2013, *MNRAS*, 431, 383, doi: [10.1093/mnras/stt174](https://doi.org/10.1093/mnras/stt174)